Research Article | Vol. 27, No. 14 | 8 Jul 2019 | OPTICS EXPRESS 19407
Optics EXPRESS

Vibrational phase imaging by stimulated Raman scattering via polarization-division interferometry

CARLO M. VALENSISE,[1] VIKAS KUMAR,[1,2] ALEJANDRO DE LA CADENA,[1] SANDRO DE SILVESTRI,[1] GIULIO CERULLO,[1] AND DARIO POLLI[1,3*]

[1] *IFN-CNR, Dipartimento di Fisica, Politecnico di Milano, Piazza Leonardo da Vinci 32, I-20133 Milano, Italy*
[2] *Present address: Universität Duisburg-Essen, Fakultät für Chemie (PC), Universitätsstr. 5, 45141 Essen, Germany*
[3] *Center for Nano Science and Technology@PoliMi, Istituto Italiano di Tecnologia, Via Giovanni Pascoli 70/3, 20133 Milano, Italy*
**dario.polli@polimi.it*

Abstract: Stimulated Raman scattering (SRS) allows chemical identification of substances based on their third-order nonlinear vibrational susceptibility $\chi^{(3)}(\omega)$. In its standard single-frequency implementation, SRS can only access the imaginary part of $\chi^{(3)}(\omega)$. Here we introduce interferometric SRS (iSRS), which has the capability to measure both the real and the imaginary parts of the nonlinear susceptibility. With respect to a standard SRS setup, iSRS simply requires the insertion of a few optical elements in the Stokes(pump) beam pathway to generate an intrinsically phase-coherent local oscillator. While preserving the acquisition speed and the simplicity of single-frequency SRS, iSRS considerably increases its information content by providing access to the vibrational phase, which allows one to distinguish overlapping species in congested spectra and is more robust with respect to noise.

1. Introduction

Coherent Raman scattering (CRS) encompasses a class of nonlinear spectroscopy and microscopy techniques for label-free identification of molecules and solids based on their characteristic vibrational fingerprints, which find a growing range of applications in life and materials sciences [1,2]. By illuminating the system with synchronized pump (at frequency ω_p) and Stokes (at frequency ω_S) pulses, whose frequency difference matches a vibrational frequency Ω of the molecule, CRS sets up a vibrational coherence which drives a nonlinear signal many orders of magnitude stronger than in the case of spontaneous Raman. In coherent anti-Stokes Raman scattering (CARS) [3] the nonlinear signal is at the anti-Stokes frequency, $\omega_{aS} = \omega_p + \Omega$, while in stimulated Raman scattering (SRS) [4] the signal is emitted at the Stokes/pump frequency, resulting in Stokes amplification and pump attenuation, called stimulated Raman gain (SRG) and stimulated Raman loss (SRL), respectively.

The CRS signal depends on the third-order nonlinear vibrational susceptibility, which can be written as $\chi^{(3)}(\omega) = \chi_R^{(3)}(\omega) + \chi_{NR}^{(3)}(\omega)$, where $\chi_R^{(3)}(\omega)$ is the resonant susceptibility, typically described by the superposition of complex Lorentzian functions corresponding to the different vibrational transitions:

$$\chi_R^{(3)}(\omega) = \sum_{k=1}^{n} \frac{A_k}{\omega - \Omega_k + i\Gamma_k}, \tag{1}$$

#364377 https://doi.org/10.1364/OE.27.019407
Journal © 2019 Received 8 Apr 2019; revised 13 Jun 2019; accepted 13 Jun 2019; published 26 Jun 2019

Optics EXPRESS

where $A_k \propto N_k \sigma_k$ and Γ_k are the effective amplitude and the linewidth respectively associated with the vibrational resonance Ω_k driven by a concentration of active scatterers N_k with cross section σ_k. The $\chi_{NR}^{(3)}$ term, on the other hand, is the real vibrationally non-resonant susceptibility generated by the electronic contributions of the molecules under study and of the surrounding environment.

Standard CRS techniques do not allow the retrieval of the full complex nonlinear susceptibility $\chi^{(3)}(\omega)$. In CARS the nonlinear signal is given by $E_{CARS}(\omega) = \chi^{(3)}(\omega) E_p^2 E_S^*$, where E_p and E_S are the pump and Stokes field amplitudes, respectively. The measured intensity is

$$I_{CARS} = \left|E_{CARS}(\omega)\right|^2 \propto \left|\chi_R^{(3)}\right|^2 + \left(\chi_{NR}^{(3)}\right)^2 + 2\chi_{NR}^{(3)} \mathrm{Re}\left(\chi_R^{(3)}\right), \qquad (2)$$

thus resulting in a complicated mixing of the real and imaginary components of the nonlinear susceptibility. SRS, on the other hand, measures the Stokes/pump intensity change, resulting in the signal $I_{SRS} \propto \mathrm{Im}(\chi_R^{(3)})$, which yields information exclusively of the imaginary part of the nonlinear susceptibility. Measurement of the complex nonlinear susceptibility, including amplitude and phase, would offer a richer spectroscopic information [5]; for example, it could be used to distinguish multiple species in a sample that, at a certain vibrational frequency, displays signals with comparable amplitudes but different phases.

When the full CARS/SRS spectrum is available [6,7], then one can retrieve both real and imaginary parts using numerical approaches, such as the Kramers-Krönig transform [8] or maximum entropy methods [9,10]. However, broadband CRS is typically slow [11] and most CRS microscopes work at a single frequency, where they achieve a very high imaging speed, up to the video rate [12,13]. A simple method allowing measurement of the complex nonlinear susceptibility for such single-frequency CRS configurations without sacrificing the acquisition speed would thus be highly beneficial for many applications in which species with overlapping vibrational resonances need to be distinguished.

The complex nonlinear susceptibility can be measured with interferometric CARS (iCARS) [14,15]. In this technique, the nonlinear signal E_{CARS} is superimposed on the detector with a phase-coherent local oscillator (LO) field E_{LO} at the anti-Stokes frequency. Under the hypothesis that $E_{LO} \gg E_{CARS}$, the resulting signal can be expressed as

$$I_{iCARS}(\omega) \propto \left|E_{CARS} + E_{LO} e^{i\Delta\phi}\right|^2 \simeq \left|E_{LO}\right|^2 + 2E_{LO}\left\{\mathrm{Re}\left[E_{CARS}\right]\cos(\Delta\phi) + \mathrm{Im}\left[E_{CARS}\right]\sin(\Delta\phi)\right\}, \qquad (3)$$

where $\Delta\phi$ is the phase difference between the LO and the CARS fields. By setting $\Delta\phi$ to 0 or $\pi/2$, iCARS enables one to measure separately the real and imaginary parts of the CARS field and thus to retrieve the full nonlinear susceptibility. Despite being spectroscopically powerful, iCARS is technically very demanding, as it requires: (i) the generation, temporal and spatial superposition of three distinct pulses (pump, Stokes and the LO at the anti-Stokes frequency); (ii) phase coherence between LO and CARS signals, which is typically achieved suppressing pathlength fluctuations by high-frequency phase modulation. iCARS has been applied in a series of pioneering papers by Offerhaus and associates, exploiting the cascaded phase-preserving chain constituted by the pump, signal and idler beams of an optical parametric oscillator [16,17], and using high-frequency modulation to circumvent mechanical phase drifts between the LO and the CARS signal, to perform imaging with vibrational phase contrast [18]. Alternatively, in single-beam CARS broadband pulse shaping in combination with double-quadrature spectral interferometry has been used to retrieve the vibrational phase

Optics EXPRESS

[19,20], and in wide-field CARS a wavefront sensor has been used to record the phase of the anti-Stokes field [21]. All these implementations have so far not found widespread application due to the complexity of the experimental apparatus. Interferometric detection has also been applied to SRS [22–24] but only in broadband configurations that are not suitable for high-speed imaging.

In this paper, we introduce interferometric SRS (iSRS), an extension of interferometric detection to single-frequency SRS, presently the mainstream CRS technique. iSRS is capable of measuring both the real and the imaginary parts of the nonlinear susceptibility and thus of retrieving the phase of vibrational transitions.

2. Experimental setup

Figure 1 shows the conceptual experimental setup for iSRS. For simplicity, we consider only the case of SRG, but the same configuration could be applied to SRL detection. It starts as a standard single-frequency SRS setup, in which narrowband, picosecond pump and Stokes pulses with parallel (vertical in our case) polarizations are synchronized, collinearly combined by a dichroic mirror and focused on the sample. The pump pulse is modulated at high frequency and the pump-induced variation of the Stokes energy, i.e. the SRG, is synchronously detected with a photodiode combined with a lock-in amplifier. iSRS simply requires the addition of a few elements to this standard setup. The Stokes arm is equipped with a common-path birefringent interferometer, similar to the one used by Orrit and associates for transient absorption microscopy of metal nanoparticles [25,26]. A half-wave-plate rotates the polarization of the beam by 45° and a block of birefringent material with vertical optical axis creates two replicas of the incoming pulse [27]. The trailing one acts as the Stokes pulse and, in the presence of SRG, its field is modified by a quantity $\Delta E_S \propto i\chi^{(3)}(\omega)\left|E_p\right|^2 E_S$. The leading one, on the other hand, is unperturbed due to lack of temporal overlap with the pump and is employed as a phase-coherent LO.

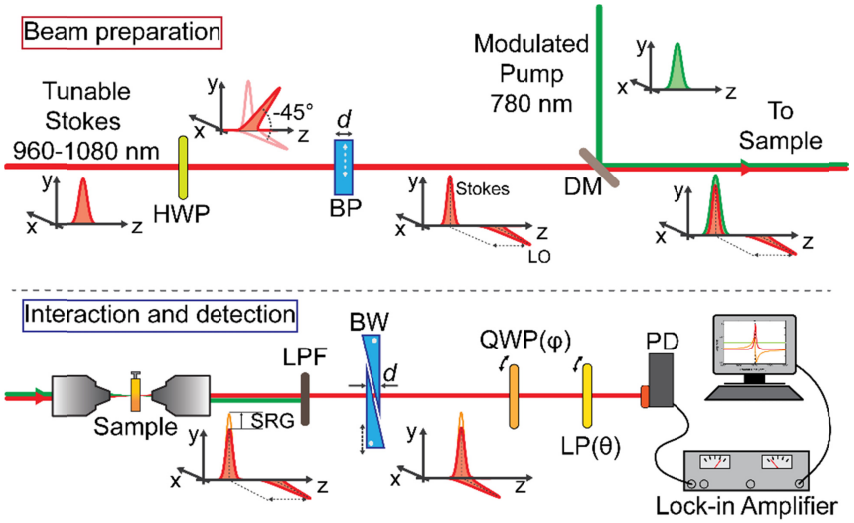

Fig. 1. Experimental setup for iSRS. HWP: Half Wave Plate; BP: birefringent plate; DM: dichroic mirror; SRG: Stimulated Raman Gain; LPF: Long-pass Filter; BW: birefringent wedges; QWP: Quarter Wave Plate; LP: Linear Polarizer; PD: Photodiode.

After the sample, the pump pulse is rejected by a spectral filter and the Stokes and LO pulses are brought back to zero relative delay by a second birefringent plate with thickness nominally identical to the first one but optical axis rotated by 90°. This plate is shaped in the form of two wedges whose overall thickness can be finely tuned by simply adjusting the

Optics EXPRESS

insertion of one wedge in the beam by transverse translation [28]. Finally, the Stokes and LO fields are made to interfere at the detector after passing through a quarter-wave plate (QWP) and a linear polarizer (LP), which are key elements to extract the complex pump-induced variation of the Stokes field ΔE_S in both its real and imaginary components.

We can express the intensity of the transmitted beam $I_{S0}(\theta,\phi)$ in the absence of SRG as (see Appendix 1 for a full analytical derivation based on Jones calculus):

$$I_{S0}(\theta,\phi) \propto \left[2-\sin(2\theta)+\sin(2(\theta-2\phi))\right], \tag{4}$$

where θ is the orientation of the transmission axis of LP and ϕ is the rotation angle of the QWP, both defined with respect to the horizontal direction. Figure 2 (a) shows a colormap of Eq. (4), displaying areas of high (yellow) and low (purple) intensity, corresponding to constructive and destructive interference of the Stokes with the LO, respectively. For a given angle of QWP (corresponding to a horizontal cut), $I_{S0}(\theta)$ follows the Malus' law. On the other hand, rotating the QWP the beam impinging on the LP changes its polarization from linear (at $\phi = 45°,135°$) to circular (at $\phi = 0°,90°$). Indeed, at $\phi = 0°,90°$ Eq. (4) simplifies into a constant value, irrespective of θ.

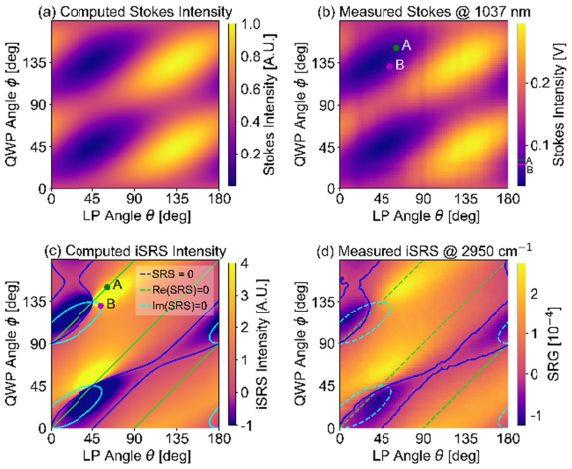

Fig. 2. Computed (panels (a) and (c)) and measured (panels (b) and (d)) $I_{S0}(\theta,\phi)$ and $I_{iSRS}(\theta,\phi)$ (see text). In panels (c) and (d) cyan green and blue curves are zero contour levels computed for $\beta(\theta,\phi)$, $\gamma(\theta,\phi)$ and $I_{iSRS}(\theta,\phi)$, respectively; "A" and "B" spots are the working points for measurements of Fig. 3 and Fig. 4.

In the presence of the pump pulse, the vertically polarized Stokes experiences SRG due to the nonlinear interaction. In the small signal limit ($\Delta E_S \ll E_S$) and considering that the modulation transfer scheme only detects the pump-induced variations of the Stokes intensity, the SRG can be expressed as (see Appendix 1):

$$\Delta I_S(\theta,\phi) = I_S - I_{S0} \propto \beta(\theta,\phi)\,\mathrm{Re}(\chi^{(3)}) + \gamma(\theta,\phi)\,\mathrm{Im}(\chi^{(3)}), \tag{5}$$

where

$$\begin{cases} \beta(\theta,\phi) = 2\sin\left[2(\theta-\phi)\right] \\ \gamma(\theta,\phi) = 2-\sin(2\theta)-\cos(2\theta) \\ \qquad\qquad +\sin\left[2(\theta-2\phi)\right]-\cos\left[2(\theta-2\phi)\right]. \end{cases} \tag{6}$$

Optics EXPRESS

Remarkably, Eq. (6) shows that it is possible to determine working points in the (θ,ϕ) phase space in which simultaneously $\beta = 0$ and $\gamma \neq 0$, or vice-versa, thus enabling the independent measurement of $\mathrm{Im}(\chi^{(3)})$ and $\mathrm{Re}(\chi^{(3)})$, respectively. The iSRS signal is finally defined as

$$I_{iSRS} = \Delta I_S(\theta,\phi) / I_{S0}. \quad (7)$$

Figure 2 (c) reports a colormap of $I_{iSRS}(\theta,\phi)$, together with the contour levels $\beta = 0$ (in green) and $\gamma = 0$ (in cyan). We note that iSRS provides regions (purple areas in Fig. 2 (c)) where $I_{iSRS} < 0$. This occurs when the interfering fields have opposite sign and the negative field is larger than the positive one, thus producing a negative interference term. Figure 2 (c) reports (in blue) the boundaries of the negative sign regions, i.e. where $I_{iSRS} = 0$, computed for an exemplary case with $\mathrm{Im}(\chi^{(3)}) = 1.05\,\mathrm{Re}(\chi^{(3)})$, where the proportionality factor was chosen to match the experimental data reported in panel (d), as discussed below. Appendix 1 reports a detailed discussion of the interferometer working principle and the full derivation of the $I_{iSRS}(\theta,\phi)$ signal. We note that the presented approach has a limited applicability when the samples under investigation show strong birefringence or diattenuation. Under such conditions, the working points of the interferometer could change location in phase space or vary between different regions in the sample in case of spatially varying birefringence and/or diattenutation.

3. Experimental results

We experimentally tested the iSRS configuration using a previously described SRS setup driven by a compact fiber laser [29,30]. The system starts with a femtosecond Er:fiber oscillator seeding two synchronized Er:doped fiber amplifiers, each providing 80-fs pulses at ~1550 nm wavelength with ~350 mW average power. The output of the first branch is frequency doubled by a long periodically poled lithium niobate (PPLN) crystal, generating ~2-ps pump pulses at ~780 nm wavelength with 120-mW average power. The second branch feeds a highly nonlinear fiber generating a supercontinuum, the long-wavelength part of which is frequency doubled in a second PPLN crystal, with a fan-out geometry, generating ~1-ps Stokes pulses with 2–5 mW average power, continuously tunable in the 930–1060 nm range. In this way, it is possible to vary the pump-Stokes frequency detuning in the 2070–3400 cm^{-1} range, which comprises the entire CH molecular vibrational region (2800–3200 cm^{-1}). The pump beam is modulated at 1 MHz by an acousto-optic modulator and the SRG is detected by a photodiode in combination with a high-frequency lock-in amplifier. A 6-mm thick birefringent YVO_4 plate is inserted in the Stokes beam to generate a LO which is anticipated by ~4ps [27]. After the sample, the delay between Stokes and LO is canceled with interferometric precision by a pair of YVO_4 wedges (apex angle 10°), whose insertion can be finely tuned via a mechanical motor [28,31]. The use of a wedge pair is crucial, as it would be very difficult to find two plates with precisely matched thickness. The QWP and the LP, which are inserted after the wedges, are also rotated through motorized mechanical stages. We note that, due to the common-path nature of the interferometer, phase stability between Stokes and LO fields is achieved effortlessly and with high fidelity.

We first tested our birefringent interferometer by measuring the Stokes intensity $I_{S0}(\theta,\phi)$, in the absence of the pump beam. The experimental colormap, reported in Fig. 2(b), is in excellent agreement with the calculated one (Fig. 2(a)). We then turned on the pump beam and measured $I_{iSRS}(\theta,\phi)$ on acetone at 2950 cm^{-1} detuning, for which the ratio of real and imaginary parts of $\chi^{(3)}$ matches the value used in the calculations. The results, shown in Fig. 2(d), are again in excellent agreement with the computed intensities (Fig. 2(c)).

As shown by Fig. 2, there are several working points of the interferometer that allow isolating the real and the imaginary part of the third-order nonlinear susceptibility. In the

Optics EXPRESS

following, we chose $(\theta,\phi)=(61°,151°)$, to measure $\mathrm{Im}(\chi^{(3)})$ and $(\theta,\phi)=(54°,131°)$ for $\mathrm{Re}(\chi^{(3)})$ (see spots "A" and "B" in Fig. 2(b-c)). These working points were selected to obtain the highest positive signals. Furthermore, we highlight the possibility of carrying out a complete measurement of the complex vibrational susceptibility in parallel, by simply duplicating the interferometric block of the setup composed by QWP and LP, after the wedge pair, and properly setting the working point of each of the two blocks.

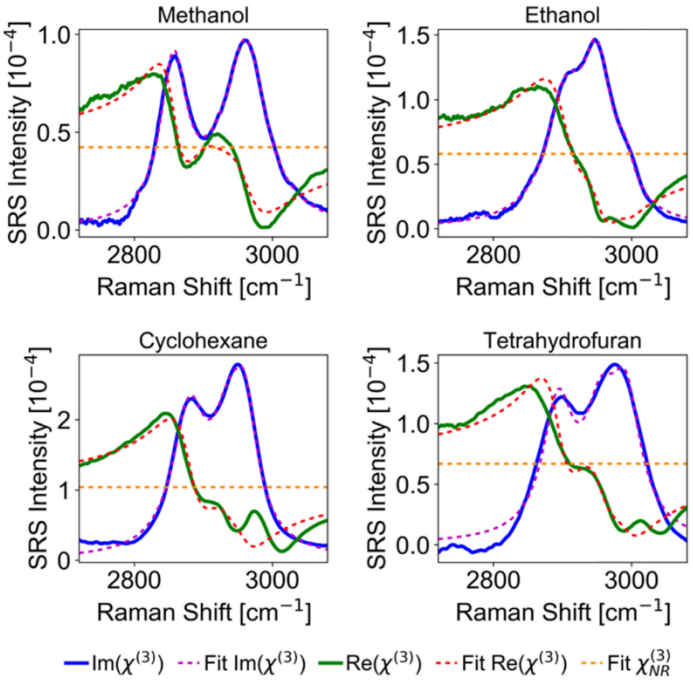

Fig. 3. Measured real (green) and imaginary (blue) SRS spectra of different solvents. Dashed red/violet lines represent fits performed with two or three terms of the sum in Eq. (1). Orange dashed lines highlight to the non-resonant background contribution.

Having verified the working principle of the interferometer, we proceeded to its application. Solid lines in Fig. 3 report real and imaginary parts of the vibrational susceptibility measured for different solvents. Experimental data were fitted by Eq. (1) with two or three resonances, keeping fixed the resonance frequencies (Ω_k) and the linewidths (Γ_k) parameters for real and imaginary parts. The fits (dashed lines in Fig. 3) show a good agreement with the data. The offset present in the $\mathrm{Re}(\chi^{(3)})$ measurements is due to the non-resonant part of the vibrational susceptibility, which is constant with respect to the Raman Shift, and indicated with dashed orange line in Fig. 3.

Finally, to show the added information content provided by iSRS, we imaged a test sample consisting of a mixture of poly-methylmethacrylate (PMMA) and polystyrene (PS) beads with 6- and 3-μm diameters, respectively. Figure 4 shows in panels (a) and (b) iSRS images of the imaginary and the real part of the nonlinear susceptibility of the sample, respectively, at a frequency 2990 cm^{-1}, intermediate between the main Raman resonances of PMMA (2953 cm^{-1}) and PS (3060 cm^{-1}). Due to the different vibrational phases of the two materials at this frequency, one observes a contrast reversal between the two images, with the PMMA (PS) beads dominating in the imaginary (real) image. Having measured the full complex nonlinear susceptibility at this frequency, one can easily calculate amplitude and phase. The image of the vibrational phase of the sample, reported in Fig. 4 (c), shows an

Optics EXPRESS

enhanced contrast between the two components, with very sharp boundaries even at the thin borders of the beads, demonstrating that iSRS provides a more robust discrimination criterion than the Raman amplitude of standard SRS setups, provided that, as explained in Ref [22], the two measurement of Real and Imaginary parts are performed with the same level of detected power. The selected working points (see. spots "A" and "B" in Fig. 2(b-c)) satisfy this condition being the measured intensities of 75 mV and 68 mV respectively. The corresponding noise variation will be therefore of the order of 5%, a difference that can be considered negligible. Finally, Fig. 4 (d) plots real and imaginary components of the signal against each other for every pixel of the image. The points are clustered in two well-defined clouds, each with its own vibrational phase, corresponding to the two chemical species composing the sample (PS along the red line with ≈20° phase, PMMA along the green line with ≈75° phase).

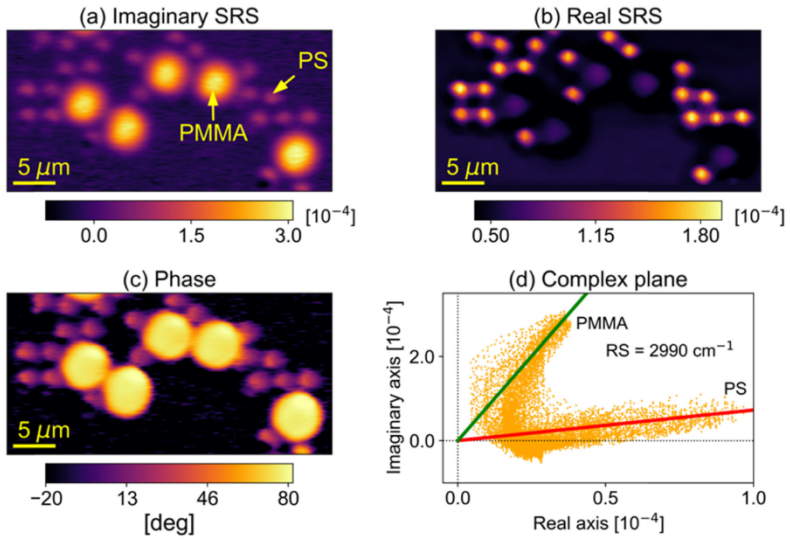

Fig. 4. Polystyrene (PS) and polymethyl methacrylate (PMMA) spheres imaged at 2990 cm^{-1} Raman Shift. (a-b) are images from imaginary and real response, respectively; (c) is the phase image produced combining (a) and (b); (d) data points scattered in the complex plane.

4. Summary

In conclusion, we have extended interferometric detection to single-frequency SRS, which is currently the mainstream CRS technique for high-speed label-free vibrational imaging. We use an in-line common-path interferometer to create an intrinsically phase-stable LO pulse which interferes with the Stokes pulse, allowing measurement of both real and imaginary components of the nonlinear Raman signal. Our approach involves minimal modifications of a standard SRS setup and in particular, if compared with iCARS, it does not require an LO pulse at a different color with respect to pump and Stokes. Access to the vibrational phase, which is more robust with respect to noise [22], significantly enhances the chemical selectivity of single-frequency SRS, since it enables one to distinguish between different overlapping vibrational resonances with comparable amplitudes but different phases.

Funding

European Research Council Consolidator Grant VIBRA (ERC-2014-CoG 648615), Horizon2020 GRAPHENE Flagship (785219), and KAUST (OSR-2016-CRG5-3017-01).

Optics EXPRESS

Appendix: Interferometer working principle

The common-path interferometer that allows one to independently measure real and imaginary parts of the $\chi^{(3)}$ vibrational susceptibility can be modeled via Jones algebra [26]. Here we report the calculations in detail. In the following, the delay between the two equally intense orthogonally polarized (along x and y directions) Stokes and LO after the sample is assumed to be already canceled out by the proper insertion of the birefringent wedges, so that only the effect of the QWP and the LP will be considered. In the absence of the pump pulse and neglecting linear absorption from the sample at the Stokes wavelength, as expected in SRS, the resulting light field of the two replicas entering the interferometer will be polarized at –45° with respect to the x direction, and it is represented by the Jones vector

$$\mathrm{E}_0 = \frac{1}{\sqrt{2}}\begin{pmatrix} -1 \\ 1 \end{pmatrix}. \tag{8}$$

LP and QWP are the two Jones matrices representing the linear polarizer and the quarter wave plate, and are defined as

$$\mathrm{LP}(\theta) = \frac{1}{2}\begin{pmatrix} 1+\cos(2\theta) & \sin(2\theta) \\ \sin(2\theta) & 1-\cos(2\theta) \end{pmatrix} \tag{9}$$

$$\mathrm{QWP}(\phi) = \frac{1}{\sqrt{2}}\begin{pmatrix} 1+i\cos(2\phi) & i\sin(2\phi) \\ i\sin(2\phi) & 1-i\cos(2\phi) \end{pmatrix} \tag{10}$$

The light intensity reaching the detector can therefore be written as

$$I_{S0}(\theta,\phi) = \left|LP(\theta)\cdot QWP(\phi)\cdot E_0\right|^2 = \frac{1}{4}(1-\sin(2\theta)+\sin(2(\theta-2\phi)) \tag{11}$$

where θ and ϕ are the angles formed by the transmission axis of the polarizer and by the optical axis of the wave plate with the x direction respectively, as shown in Fig. (5).

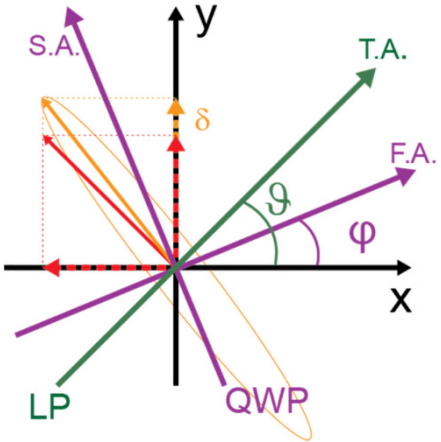

Fig. 5. Reference frame for interferometer model. Input electric field in absence of the pump beam is represented by the red arrow, reported together with its projections onto the reference x-y axes (dashed arrows). Purple axes represent the fast axis (F.A.) and slow axis (S.A.) directions of the QWP, while the green arrow is the transmission axis (T.A.) of the polarizer. The orange arrow represents the electric field modified by the SRG signal due to interaction of the pump pulse, and the ellipse traces its trajectory on the x-y plane for different values of θ

Optics EXPRESS

and ϕ. The tiny SRG signal on the vertically polarized component is exaggerated in scale for clarity.

Values of $I_{S0}(\theta,\phi)$ are reported in Figure 2(a). In presence of the SRG signal due to interaction with the pump pulse in the sample, the Stokes electric field entering the interferometer is modified as

$$\mathrm{E}=\frac{1}{\sqrt{2}}\begin{pmatrix}-1\\1+\delta\end{pmatrix}, \tag{12}$$

where δ is a complex quantity, responsible for SRG, that modifies the vertical replica. Due to the complex nature of δ, the new resulting field E is slightly rotated (shown by the yellow arrow) with respect to the its original direction (that of E_0, along the red arrow) and acquires a small elliptical polarization, represented as the orange ellipse in Fig. 5. In analogy to Eq. (11), the modified intensity reaching the detector as a function of θ, ϕ and δ is computed as

$$\begin{aligned} I_S(\theta,\phi,\delta) &= \left|\mathrm{LP}(\theta)\cdot\mathrm{QWP}(\phi)\cdot\mathrm{E}\right|^2 = \\ &= \frac{1}{4}\left[2-\sin(2\theta)+\sin(2(\theta-2\phi))\right]+ \\ &-\frac{1}{2}\left[\sin(2(\theta-\phi))\right]\mathrm{Im}(\delta) \\ &+\frac{1}{4}\left[2-\cos(2\theta)-\cos(2(\theta-2\phi))-\sin(2\theta)+\sin(2(\theta-2\phi))\right]\mathrm{Re}(\delta) \\ &+\frac{1}{8}\left[2-\cos(2\theta)-\cos(2(\theta-2\phi))\right]|\delta|^2 . \end{aligned} \tag{13}$$

Due to the modulation transfer in iSRS, the output signal after the lock-in amplifier will be proportional to the intensity difference given as

$$\Delta I_S(\theta,\phi,\delta)=I_S(\theta,\phi,\delta)-I_{S0}(\theta,\phi), \tag{14}$$

such that the first term of Eq. (13) is canceled out, being independent of δ. Moreover, in the small signal limit ($\delta I_S \ll I_S$) we can neglect the last term, proportional to $|\delta|^2$. Thus, the effective signal is

$$\begin{aligned} \Delta I_S(\theta,\phi,\delta) &= -\frac{1}{2}\left[\sin(2(\theta-\phi))\right]\mathrm{Im}(\delta) \\ &+\frac{1}{4}\left[2-\cos(2\theta)-\cos(2(\theta-2\phi))-\sin(2\theta)+\sin(2(\theta-2\phi))\right]\mathrm{Re}(\delta) \end{aligned} \tag{15}$$

Which, considering that $\delta \propto -i\chi^{(3)}$, can be rewritten as

$$\begin{aligned} \Delta I_S(\theta,\phi,\chi^{(3)}) &\propto \frac{1}{2}\left[\sin(2(\theta-\phi))\right]\mathrm{Re}(\chi^{(3)}) \\ &+\frac{1}{4}\left[2-\cos(2\theta)-\cos(2(\theta-2\phi))-\sin(2\theta)+\sin(2(\theta-2\phi))\right]\mathrm{Im}(\chi^{(3)}) \end{aligned} \tag{16}$$

which can finally be rearranged as

$$\Delta I_S \propto \beta(\theta,\phi)\,\mathrm{Re}(\chi^{(3)})+\gamma(\theta,\phi)\,\mathrm{Im}(\chi^{(3)}) \tag{17}$$

Optics EXPRESS

which corresponds to Eq. (5) in the paper. The contour levels $\beta = 0$ (in green) and $\gamma = 0$ (in cyan) are reported in Fig. 2 (c) and also in Fig. 3 (d). Finally, the iSRS signal is defined as reported in Eq. (8).

References

1. J.-X. Cheng and X. S. Xie, Coherent Raman Scattering Microscopy (CRC Press, Boca Raton, FL, 2013).
2. J.-X. Cheng and X. S. Xie, "Vibrational spectroscopic imaging of living systems: An emerging platform for biology and medicine," Science **350**(6264), aaa8870 (2015).
3. A. Zumbusch, G. R. Holtom, and X. S. Xie, "Three-Dimensional Vibrational Imaging by Coherent Anti-Stokes Raman Scattering," Phys. Rev. Lett. **82**(20), 4142–4145 (1999).
4. C. W. Freudiger, W. Min, B. G. Saar, S. Lu, G. R. Holtom, C. He, J. C. Tsai, J. X. Kang, and X. S. Xie, "Label-free biomedical imaging with high sensitivity by stimulated Raman scattering microscopy," Science **322**(5909), 1857–1861 (2008).
5. M. Jurna, E. T. Garbacik, J. P. Korterik, J. L. Herek, C. Otto, and H. L. Offerhaus, "Visualizing resonances in the complex plane with vibrational phase contrast coherent anti-Stokes Raman scattering," Anal. Chem. **82**(18), 7656–7659 (2010).
6. C. H. Camp, Jr., Y. J. Lee, J. M. Heddleston, C. M. Hartshorn, A. R. Hight Walker, J. N. Rich, J. D. Lathia, and M. T. Cicerone, "High-speed coherent Raman fingerprint imaging of biological tissues," Nat. Photonics **8**(8), 627–634 (2014).
7. M. S. Alshaykh, C.-S. Liao, O. E. Sandoval, G. Gitzinger, N. Forget, D. E. Leaird, J.-X. Cheng, and A. M. Weiner, "High-speed stimulated hyperspectral Raman imaging using rapid acousto-optic delay lines," Opt. Lett. **42**(8), 1548–1551 (2017).
8. Y. Liu, Y. J. Lee, and M. T. Cicerone, "Broadband CARS spectral phase retrieval using a time-domain Kramers-Kronig transform," Opt. Lett. **34**(9), 1363–1365 (2009).
9. E. M. Vartiainen, "Phase retrieval approach for coherent anti-Stokes Raman scattering spectrum analysis," J. Opt. Soc. Am. B **9**(8), 1209–1214 (1992).
10. E. M. Vartiainen, H. A. Rinia, M. Müller, and M. Bonn, "Direct extraction of Raman line-shapes from congested CARS spectra," Opt. Express **14**(8), 3622–3630 (2006).
11. D. Polli, V. Kumar, C. M. Valensise, M. Marangoni, and G. Cerullo, "Broadband Coherent Raman Scattering Microscopy," Laser Photonics Rev. **12**(9), 1800020 (2018).
12. C. L. Evans, E. O. Potma, M. Puoris'haag, D. Côté, C. P. Lin, and X. S. Xie, "Chemical imaging of tissue in vivo with video-rate coherent anti-Stokes Raman scattering microscopy," Proc. Natl. Acad. Sci. U.S.A. **102**(46), 16807–16812 (2005).
13. B. G. Saar, C. W. Freudiger, J. Reichman, C. M. Stanley, G. R. Holtom, and X. S. Xie, "Video-rate molecular imaging in vivo with stimulated Raman scattering," Science **330**(6009), 1368–1370 (2010).
14. C. L. Evans, E. O. Potma, and X. S. Xie, "Coherent anti-stokes raman scattering spectral interferometry: determination of the real and imaginary components of nonlinear susceptibility $\chi(3)$ for vibrational microscopy," Opt. Lett. **29**(24), 2923–2925 (2004).
15. E. O. Potma, C. L. Evans, and X. S. Xie, "Heterodyne coherent anti-Stokes Raman scattering (CARS) imaging," Opt. Lett. **31**(2), 241–243 (2006).
16. M. Jurna, J. P. Korterik, C. Otto, and H. L. Offerhaus, "Shot noise limited heterodyne detection of CARS signals," Opt. Express **15**(23), 15207–15213 (2007).
17. M. Jurna, J. P. Korterik, C. Otto, J. L. Herek, and H. L. Offerhaus, "Background free CARS imaging by phase sensitive heterodyne CARS," Opt. Express **16**(20), 15863–15869 (2008).
18. M. Jurna, J. P. Korterik, C. Otto, J. L. Herek, and H. L. Offerhaus, "Vibrational phase contrast microscopy by use of coherent anti-Stokes Raman scattering," Phys. Rev. Lett. **103**(4), 043905 (2009).
19. S.-H. Lim, A. G. Caster, and S. R. Leone, "Single-pulse phase-control interferometric coherent anti-Stokes Raman scattering spectroscopy," Phys. Rev. A **72**, 041803 (2005).
20. A. Wipfler, J. Rehbinder, T. Buckup, and M. Motzkus, "Full characterization of the third-order nonlinear susceptibility using a single-beam coherent anti-Stokes Raman scattering setup," Opt. Lett. **37**(20), 4239–4241 (2012).
21. P. Berto, D. Gachet, P. Bon, S. Monneret, and H. Rigneault, "Wide-field vibrational phase imaging," Phys. Rev. Lett. **109**(9), 093902 (2012).
22. F. E. Robles, M. C. Fischer, and W. S. Warren, "Dispersion-based stimulated Raman scattering spectroscopy, holography, and optical coherence tomography," Opt. Express **24**(1), 485–498 (2016).
23. F. E. Robles, K. C. Zhou, M. C. Fischer, and W. S. Warren, "Stimulated Raman scattering spectroscopic optical coherence tomography," Optica **4**(2), 243–246 (2017).
24. V. Kumar, A. De la Cadena, A. Perri, F. Preda, N. Coluccelli, G. Cerullo, and D. Polli, "Complex vibrational susceptibility by interferometric Fourier transform stimulated Raman scattering," APL Photonics **3**(9), 092403 (2018).
25. M. A. van Dijk, M. Lippitz, and M. Orrit, "Detection of acoustic oscillations of single gold nanospheres by time-resolved interferometry," Phys. Rev. Lett. **95**(26), 267406 (2005).
26. M. A. van Dijk, M. Lippitz, D. Stolwijk, and M. Orrit, "A common-path interferometer for time-resolved and shot-noise-limited detection of single nanoparticles," Opt. Express **15**(5), 2273–2287 (2007).

Optics EXPRESS

27. F. Crisafi, V. Kumar, T. Scopigno, M. Marangoni, G. Cerullo, and D. Polli, "In-line balanced detection stimulated Raman scattering microscopy," Sci. Rep. **7**(1), 10745 (2017).
28. D. Brida, C. Manzoni, and G. Cerullo, "Phase-locked pulses for two-dimensional spectroscopy by a birefringent delay line," Opt. Lett. **37**(15), 3027–3029 (2012).
29. M. Marangoni, A. Gambetta, C. Manzoni, V. Kumar, R. Ramponi, and G. Cerullo, "Fiber-format CARS spectroscopy by spectral compression of femtosecond pulses from a single laser oscillator," Opt. Lett. **34**(21), 3262–3264 (2009).
30. A. Gambetta, V. Kumar, G. Grancini, D. Polli, R. Ramponi, G. Cerullo, and M. Marangoni, "Fiber-format stimulated-Raman-scattering microscopy from a single laser oscillator," Opt. Lett. **35**(2), 226–228 (2010).
31. F. Preda, A. Oriana, J. Réhault, L. Lombardi, A. C. Ferrari, G. Cerullo, and D. Polli, "Linear and nonlinear spectroscopy by a common-path birefringent interferometer," IEEE J. Sel. Top. Quantum Electron. **23**(3), 88–96 (2017).